


Time-dependent Hartree-Fock study of quasifission trajectories in reactions forming ^{294}Og

P. McGlynn and C. Simenel 

Department of Fundamental and Theoretical Physics and Department of Nuclear Physics and Accelerator Applications, Research School of Physics, Australian National University, Canberra, Australian Capital Territory 2600, Australia

 (Received 15 February 2023; revised 27 April 2023; accepted 15 May 2023; published 25 May 2023)

Background: Fission modes in superheavy nuclei are expected to be impacted by quantum shell effects. Similar shell effects may be present in quasifission reactions, acting to hinder the mass equilibration process in heavy-ion collisions.

Purpose: To investigate quasifission mechanisms in five different reactions forming ^{294}Og as a compound nucleus and compare quasifission trajectories with predicted fission modes.

Methods: The potential energy surface (PES) of ^{294}Og is calculated using the static Hartree-Fock approach with BCS pairing correlations. Quasifission trajectories for central collisions at various energies are studied with the time-dependent Hartree-Fock theory.

Results: The exit channel strongly depends on initial mass asymmetry and orientation, but it only exhibits small dependencies in the reaction energy. The $^{48}\text{Ca} + ^{246}\text{Cf}$ reaction is affected by the PES topography, leading to either fusion or asymmetric fission. $^{126}\text{Sn} + ^{168}\text{Er}$ reactions exhibit large total kinetic energies and compact scission configurations, which could be interpreted as an effect of the $Z = 50$ spherical magic gap.

Conclusions: Quasifission trajectories can be interpreted in terms of the underlying PES for low excitation energies. Future investigations of quasifission with temperature- and angular-momentum-dependent PES could be considered.

DOI: [10.1103/PhysRevC.107.054614](https://doi.org/10.1103/PhysRevC.107.054614)

I. INTRODUCTION

Fission of atomic nuclei is one of the most complex nuclear reaction processes. Numerous experiments have been carried out in the past on fission of long-lived actinides induced by neutron and electromagnetic probes. The past two decades have also seen major experimental efforts to study fission mechanisms away from stability with relativistic beams, multi-nucleon transfer, and fusion reactions [1,2]. However, some regions of the nuclear chart remain difficult to access for the purpose of fission investigations, such as neutron-rich nuclei relevant to fission recycling in the r-process [3] and superheavy nuclei (SHN) which could have a superasymmetric fission mode (or cluster radioactivity) [4–10], although no conclusive experimental evidence of the existence of this mode have been found so far [11].

Despite recent progresses in microscopic approaches [12], the theoretical description of fission remains also very challenging [13]. Many theoretical approaches use potential energy surfaces as a major ingredient to predict final fragment properties, such as their mass and charge distributions. In particular, quantum shell effects in the compound system [14–17] and in the fragments [17–19] produce fission valleys in the potential energy surface (PES) that are usually associated with asymmetric fission modes.

Similar shell effects could also affect the formation of fragments in quasifission reactions [20–26]. Quasifission occurs when two heavy ions collide, fully dissipate their relative kinetic energy, and transfer nucleons from the heavy fragment

to the lighter one within a few zeptoseconds (10^{-21} s) to a few tens of zeptoseconds [27–29] (see also Ref. [30] for a recent experimental review on quasifission). This slow mass drift towards symmetry could eventually be stopped by shell effects in the fragments.

Naturally, there is no guarantee that the resulting quasifission modes are the same as in fission. Experimentally, properties of quasifission fragments can be obtained by comparing reactions forming similar compound nuclei with different entrance channels. Indeed, the most asymmetric entrance channels are expected to exhibit less quasifission [31–33]. Asymmetric modes could then be observed in quasifission while being absent (or with negligible yield) in fusion-fission reactions [31]. Nevertheless, recent time-dependent Hartree-Fock (TDHF) calculations predicted strong similarities between quasifission fragments produced in $^{50}\text{Ca} + ^{176}\text{Yb}$ and fission fragments of the ^{226}Th compound nucleus [34], indicating that both mechanisms are affected by similar shell effects.

In principle, quasifission reactions could then be used to explore regions of the PES, including those relevant to fission. In particular, one can use the fact that different entrance channels (forming the same compound nucleus) lead to different “entry points” on the PES (configurations obtained just after full dissipation of the initial kinetic energy) to search, through quasifission, for different fission valleys. The PESs used in fission modeling, however, are often constructed using approximations that do not hold, in principle, in the case of quasifission. These approximations include, e.g., axial

symmetry, zero angular momentum, and zero temperature (although PESs at finite temperatures are sometimes considered [35,36]). It is not clear, then, if the evolution of a system undergoing quasifission can be interpreted in terms of the topography (barriers, valleys, ...) of the PES used in fission studies.

Here, theoretical predictions of fission and quasifission modes in reactions forming ^{294}Og as a compound nucleus are presented. ^{294}Og is the heaviest synthesized even-even nucleus so far and its fission modes have been studied theoretically by several groups (see, e.g., Refs. [5,8,10]). In particular, it is predicted to exhibit a superasymmetric mode driven by the $Z = 82$ magic shell gap. Quasifission reactions are also often studied in reactions that would form a SHN as compound nucleus (if they were to fuse) [30].

The properties of the PES of ^{294}Og are investigated in Sec. II A. Static and time-dependent calculations were performed in the framework of Skyrme-Hartree-Fock theory with BCS pairing, as discussed in Sec. II B. In Sec. III the fission potential energy surface is analyzed. Simulations of $^{48}\text{Ca} + ^{246}\text{Cf}$, $^{86}\text{Kr} + ^{208}\text{Pb}$, and $^{126}\text{Sn} + ^{168}\text{Er}$ heavy-ion collisions leading to quasifission are presented in Sec. IV. Fission and quasifission properties are further discussed in Sec. V. Conclusions are drawn in Sec. VI.

II. METHODS AND NUMERICAL DETAILS

A. Potential energy surface

The PES was calculated using the static Hartree-Fock + BCS code SKYAX [37]. The code solves the Hartree-Fock equations with BCS pairing correlations and constraints on multipole moments. Axial symmetry is imposed to increase computational efficiency. The spatial grid used in these calculations has a 1-fm spacing in both the radial and the axial coordinates r and z and spans $-64.5 \text{ fm} \leq z \leq 64.5 \text{ fm}$, $r \leq 40 \text{ fm}$.

All calculations were performed with the SLy4d parametrization of the Skyrme energy-density functional [38] with density-dependent BCS pairing. Each point in the PES was computed by applying constraints on the quadrupole moment

$$Q_{20} = \sqrt{\frac{5}{16\pi}} \int d^3r \rho(\mathbf{r})(2z^2 - x^2 - y^2)$$

and the octupole moment

$$Q_{30} = \sqrt{\frac{7}{16\pi}} \int d^3r \rho(\mathbf{r})[2z^3 - 3z(x^2 + y^2)]$$

and solving to find the minimal energy configuration satisfying those constraints.

The adiabatic fission path is determined from the minimum energy path to scission. It is obtained by imposing a constraint on Q_{20} only while leaving Q_{30} free to vary. The constraints themselves were applied via a damped Lagrange multiplier approach which forces the converged state to have a specific expectation value for each constrained multipole moment.

Such calculations were performed for a grid of Q_{20} and Q_{30} values ranging from 0 to 270 b and from 0 to 110 $b^{3/2}$ with a

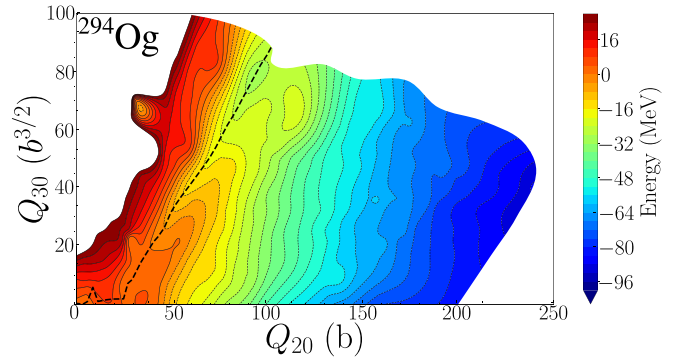


FIG. 1. Zero-temperature potential energy surface of ^{294}Og . Energy E is relative to the ground-state energy of -2071.4 MeV . The dashed line corresponds to the asymmetric adiabatic path to scission.

spacing of 2 b and $2 b^{3/2}$, respectively. In some regions of the PES the grid is denser as multiple points were calculated to improve convergence; this is done prescriptively in regions where convergence is difficult, such as near the scission line [39]. The scission line itself is defined from the density of the neck between the fragments. Here, we consider that scission occurs when the neck density is below $0.08 \text{ nucleons/fm}^3$, i.e., approximately half the nuclear saturation density.

The resulting PES of ^{294}Og is shown in Fig. 1. It was generated by interpolation of all the converged points with a radial basis function technique. The asymmetric one-dimensional path (dashed line) was determined by performing successive calculations with constraints in Q_{20} (leaving Q_{30} free) and increasing the value of Q_{20} by a step of 1 b.

B. Time-dependent Hartree-Fock simulations

Quasifission mechanisms in reactions forming the ^{294}Og compound nucleus were investigated with the TDHF code SKY3D [40,41]. A three-dimensional Cartesian grid with 1-fm mesh spacing was used. No spatial symmetries were assumed. The Skyrme energy-density functional and the pairing functional are the same as those in the PES calculations.

The collision partners were assumed to be in their ground state in the initial configuration. The ground states were obtained by solving the static Hartree-Fock equations with BCS pairing correlations inside a $28 \times 28 \times 28 \text{ fm}^3$ box. The nuclei were then placed in a larger box of $84 \times 28 \times 28 \text{ fm}^3$ with an initial distance of 56 fm between their centers of mass. A Galilean boost was then applied on each nucleus with opposite linear momenta and zero angular momentum. When one nucleus is initially axially deformed, different orientations of the deformation axis with respect to the collision axis were considered.

The TDHF equations were solved iteratively with a time step of $0.2 \text{ fm}/c$. The frozen occupation approximation was used; i.e., the initial single-particle occupation numbers issued by the static BCS calculations were kept constant in time. See Refs. [42–47] for reviews of TDHF calculations applied to nuclear dynamics. An example of evolution of isodensity surfaces in $^{126}\text{Sn} + ^{168}\text{Er}$ at a center-of-mass energy of $E_{\text{c.m.}} = 416 \text{ MeV}$ is given in Fig. 2.

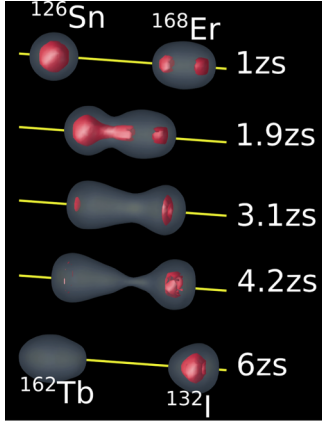


FIG. 2. Isodensity surfaces at half nuclear saturation $\rho_0/2 = 0.08 \text{ fm}^{-3}$ (translucent gray) and at saturation density $\rho_0 = 0.16 \text{ fm}^{-3}$ (opaque red), as computed with SKY3D for a quasifission reaction $^{126}\text{Sn} + ^{168}\text{Er}$ at a center-of-mass energy of $E_{\text{c.m.}} = 416 \text{ MeV}$. The collision axis is represented by the yellow solid line. The final fragments are determined based on the average numbers of protons and neutrons.

The density in the neck between the fragments was used to determine the contact time, defined as the duration of neck density exceeding half the nuclear saturation density ($\rho_0/2 = 0.08 \text{ fm}^{-3}$). The neck location was identified as the minimum density along the collision axis and located between the two largest maxima. After complete reseparation, the sum of the Coulomb interaction energy between the fragments and their kinetic energies becomes constant and was used to define the total kinetic energy (TKE) [48] (see also Refs. [49–51] for similar calculations of the TKE in fission). The numbers of protons and neutrons in the primary fragments are then determined from integration of neutron and proton densities on each side of the neck.

III. FISSION MODES

The PES shown in Fig. 1 exhibits several structures affecting fission properties of ^{294}Og . A clear valley around the adiabatic asymmetric fission path (dashed line) is observed. It starts just before the second barrier (located at $Q_{20} \simeq 35 \text{ b}$) and goes all the way to scission with the formation of a heavy fragment near the doubly magic ^{208}Pb nucleus, in agreement with earlier studies [4–9]. The height of the fission barrier is likely to be overestimated since the static calculations ignored triaxial shapes [52,53]. The relatively shallow and wide symmetric valley (along $Q_{30} = 0$), which also starts after the second barrier, is the only other valley observed in the PES.

All paths exhibit a rapid descent of the potential toward scission due to the large Coulomb repulsion between the fragments. The latter is larger for symmetric fragments, thus leading to a more rapid change in energy with increasing Q_{20} along the symmetric path. Finally, it is also observed that the scission configuration in the asymmetric mode occurs at relatively small values of Q_{20} . This can be interpreted as an effect of the heavy fragment (^{208}Pb) magicity leading to a compact scission configuration. Note that, as a result, the

TABLE I. Systems studied with TDHF in this work. Coulomb barriers V_B are from Ref. [55].

System	V_B (MeV)
$^{48}\text{Ca} + ^{246}\text{Cf}$	235.5
$^{86}\text{Kr} + ^{208}\text{Pb}$	342.6
$^{126}\text{Sn} + ^{168}\text{Er}$	387.4

production of magic fragments is usually associated with large TKE [54].

IV. QUASIFISSION SIMULATIONS

A. Initial conditions

It is unknown prior to running a TDHF calculation if the system will undergo quasifission or another reaction mechanism such as quasielastic scattering or fusion. It is then necessary to search for quasifission signatures for a range of initial conditions. These could include various collision partners, center-of-mass energies, angular momenta, and orientations in the case of deformed nuclei.

Here, TDHF investigations of quasifission reactions were performed for the systems given in Table I, all leading to the formation of ^{294}Og compound nucleus in the case of fusion. These calculations were performed for a range of energies around the Coulomb barrier V_B . Only central collisions were considered to avoid introducing angular momentum into the system, allowing for a comparison (in Sec. IV C) with fission paths on the PES that were computed for zero orbital angular momentum.

Choosing central collisions also prevents, in some cases, the system from exploring triaxial shapes, allowing for better comparison with the PES that is built assuming axial symmetry. Note that ^{246}Cf and ^{168}Er are prolately deformed. Both the tip and the side orientations, associated with their deformation axis being parallel and perpendicular to the collision axis, respectively, were considered. However, the fact that the side orientation is not axially symmetric could imply that the corresponding trajectories may be sensitive to a different PES including triaxial shapes.

B. Quasifission signatures

The TDHF approach has been extensively used to investigate quasifission mechanisms in the past decade [24,29,56–66]. Three main observables are commonly used to characterize quasifission in such calculations: contact times, TKE, and final mass asymmetries of the fragments.

1. Contact times

Although contact times are not directly accessible experimentally, they can be inferred through mass-angle distributions [27,28] as well as neutron emission [67]. Quasifission contact times typically exceed a few zeptoseconds. Quasifission outcomes were then searched for up to 30-zs contact times. Longer contact times lead to either fusion or

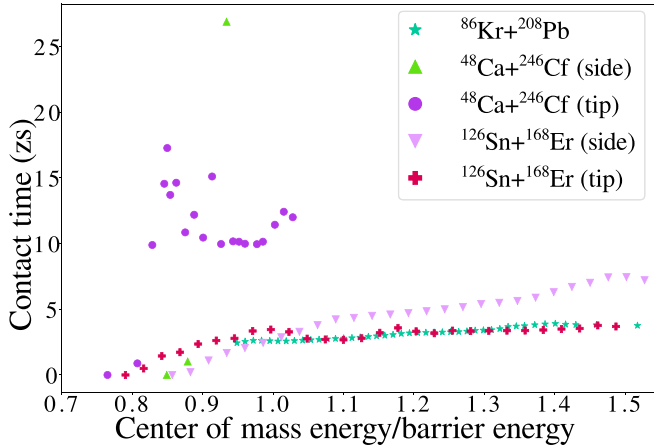


FIG. 3. Contact time as a function of center-of-mass energy with respect to the Coulomb barrier V_B .

formation of fragments in a process termed “slow quasifission” [30]. Earlier TDHF studies of quasifission with actinide targets showed that such long contact times are more easily found with the side orientation [24,56,57,61,63]. This can be attributed to the fact that these configurations are more compact at contact, thus favoring the formation of a compound nucleus. Similar results were obtained here in $^{48}\text{Ca} + ^{246}\text{Cf}$ at above barrier energies and with the side configuration. Quasifission is only found for this system and orientation for a small range of energies around 210–230 MeV (see Table II–VI in the Appendix).

Figure 3 shows the evolution of contact times as a function of center-of-mass energy normalized to the Coulomb barrier V_B . The contact time increases rapidly near the energy where contact first occurs. For spherical systems, this happens near V_B . For deformed systems, however, this threshold energy depends on the orientation, with tip collisions reaching contact at energies lower than those of side collisions. After a rapid increase at low energy, contact times either plateau or increase slowly with energy. The most asymmetric reaction, $^{48}\text{Ca} + ^{246}\text{Cf}$, leads to the longest contact times ($\approx 10\text{--}15$ zs for the tip orientation and $\gtrsim 15$ zs for the side one). As is discussed later, these longer contact times are associated with more significant mass transfer between the reactants.

2. Total kinetic energy

Another signature of quasifission is given by the final TKE of the fragments which is expected to follow Viola systematics [68,69]. Indeed, the initial kinetic energy of the fragments is expected to be fully damped in quasifission. Nevertheless, fluctuations around Viola systematics could occur, e.g., because of different orientations of deformed nuclei at contact [57,60].

The evolution of the TKE with the center-of-mass energy is shown in Fig. 4. Each system exhibits essentially no or little dependence of the TKE with energy. This indicates that the initial kinetic energy is fully damped. This damping is confirmed by their relatively good agreement with the Viola systematics [69] as seen in Fig. 5 showing the TKE as a

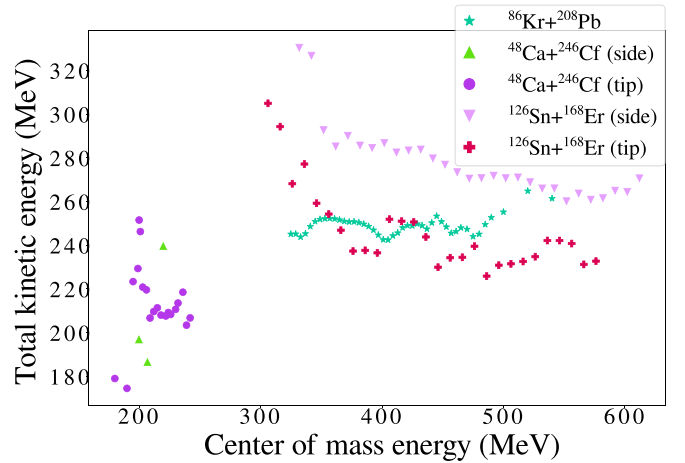


FIG. 4. Total kinetic energy as a function of center-of-mass energy.

function of the mass ratio defined as the ratio of the primary fragment mass over the compound nucleus mass.

However, a significant deviation from the Viola systematics is observed in $^{126}\text{Sn} + ^{168}\text{Er}$ reactions that encounter no or little mass transfer. In this case, one could expect the influence from the spherical shell effects in the tin region to remain. The resulting compact configuration at scission would then be associated with larger TKE, as in the case of fission.

3. Mass asymmetry

Finally, quasifission is usually associated with a large mass transfer between the fragments induced by a slow mass equilibration. Although the production of symmetric fragments requires contact times of the order of 20 zs [29], partial equilibration associated with smaller contact times is often observed. The latter could be induced by shell effects in the fragments, preventing further transfer to occur. Note that “inverse quasifission” mechanisms (leading to more mass

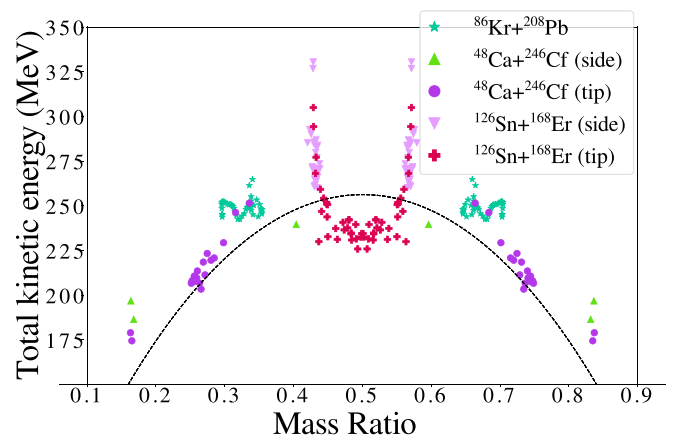


FIG. 5. Total kinetic energy as a function of fragment mass ratio (see text). The black dashed line corresponds to Viola systematics [69].

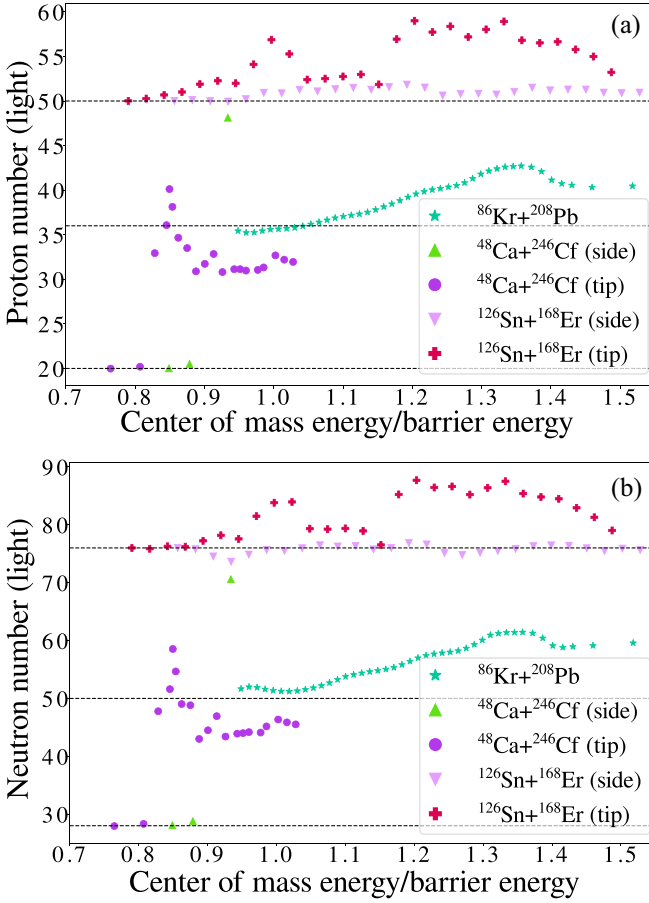


FIG. 6. (a) Proton and (b) neutron numbers of the final (light) primary fragments. Horizontal lines correspond to the proton and neutron numbers of the original light fragments.

asymmetric fragments) induced by shell [70] or orientation [71] effects have been also predicted.

The number of protons and neutrons of the outgoing primary fragments produced in quasifission are shown in Fig. 6 as a function of center-of-mass energy. All systems encounter some degree of mass equilibration, although the $^{126}\text{Sn} + ^{168}\text{Er}$ side collisions barely lead to any transfer. This could be interpreted as an influence of the magic shell $Z = 50$ in tin isotopes. Collisions with the tip of ^{168}Er , however, seem to force the Sn fragments out of their magic stability, leading to near-symmetric primary fragments.

$^{48}\text{Ca} + ^{246}\text{Cf}$ collisions are those that lead to the largest amount of mass transfer. This is compatible with the larger contact times obtained for this system (see Fig. 3). The lowest-energy quasifissions seem to favor the formation of heavy fragments near the ^{208}Pb doubly magic nucleus. At higher energy, however, the heavy fragment is found typically with $Z_H \approx 86$ protons and $N_H \approx 131$ neutrons, while the light one has $Z_L \approx 31$ and $N_L \approx 44$. Possible shell effects that could be responsible for the formation of these fragments are the octupole deformed shell effects at $Z = 84$ and 88 (see, e.g., Ref. [72]), and elongated shell effects at $N = 42$ – 46 [73,74].

Finally, a relatively smooth transition is observed in the $^{86}\text{Kr} + ^{208}\text{Pb}$ system. At lower energies, little transfer is ob-

served, which could be interpreted as an influence of the doubly magic ^{208}Pb . With increasing energies, however, the heavy fragment is formed with $Z_H \approx 76$ and $N_H \approx 117$, corresponding to a light fragment with $Z_L \approx 42$ and $N_L \approx 60$. This repartition could be influenced by elongated deformed shell effects near $Z = 42$ (see, e.g., the Supplemental Material of Ref. [75]). In both $^{86}\text{Kr} + ^{208}\text{Pb}$ and $^{48}\text{Ca} + ^{246}\text{Cf}$, the shell effects associated with ^{208}Pb seem to rapidly wash out with energy.

C. Quasifission trajectories in the $Q_{20} - Q_{30}$ plane

In the interest of comparison between fission and quasifission modes, the quasifission “trajectories” have been determined in the Q_{20} – Q_{30} plane and overlaid with the PES of Fig. 1. Note that, as the values of Q_{30} sometime become negative, the absolute value $|Q_{30}|$ was used. The results are plotted in Fig. 7 for each system. The primary goal of this comparison is to see if these trajectories are affected by the PES topography, keeping in mind that the PES has been determined at zero temperature while finite excitation energies are expected in quasifission. In addition, the axial symmetry that was assumed to construct the PES is broken in the TDHF initial conditions for $^{48}\text{Ca} + ^{246}\text{Cf}$ and $^{126}\text{Sn} + ^{168}\text{Er}$ with side orientation.

Each trajectory can be separated into three parts: (i) incoming trajectory determined by kinematics, (ii) fragments in contact, and (iii) postscission outgoing trajectory (also determined by kinematics). The separation between (i) and (ii) is expected to occur near contact, defined here as the time when the neck density reaches 0.08 fm^{-3} (approximately half the saturation density) and represented by stars in Fig. 7. At this point the kinetic energy rapidly dissipates within a timescale of ≈ 1 – 2 zs [34], leading to the entry point where the system is expected to be most sensitive to the PES topography.

However, energy dissipation is difficult to quantify in a manner that is agnostic of entrance channel. In order to compare systems uniformly, the entry point is simply defined here as the first time when the neck density exceeds 0.14 fm^{-3} . The choice of 0.14 fm^{-3} is arbitrary but motivated by inspection of both trajectories and kinetic energy from the numerical results. The resulting entry point densities from TDHF are compared in Fig. 8 with static configurations of similar deformation parameters β_2 and β_3 defined as

$$\beta_i = \frac{4\pi}{3A(r_0 A^{1/3})^i} Q_{i0},$$

with $r_0 = 1.2 \text{ fm}$, for several initial conditions. Overall, static and dynamic shapes exhibit strong similarities, although the agreement is somewhat worse with side collisions due to triaxiality induced by the initial orientation.

I. $^{48}\text{Ca} + ^{246}\text{Cf}$

Figure 7(a) shows the trajectories for $^{48}\text{Ca} + ^{246}\text{Cf}$. The incoming trajectories for side and tip orientations are parallel to each other, with the side one associated with smaller Q_{20} and thus leading to more compact configurations. The entry points for the side orientation have Q_{20} values smaller than those of the second barrier (located at $Q_{20} \approx 33 \text{ b}$ and

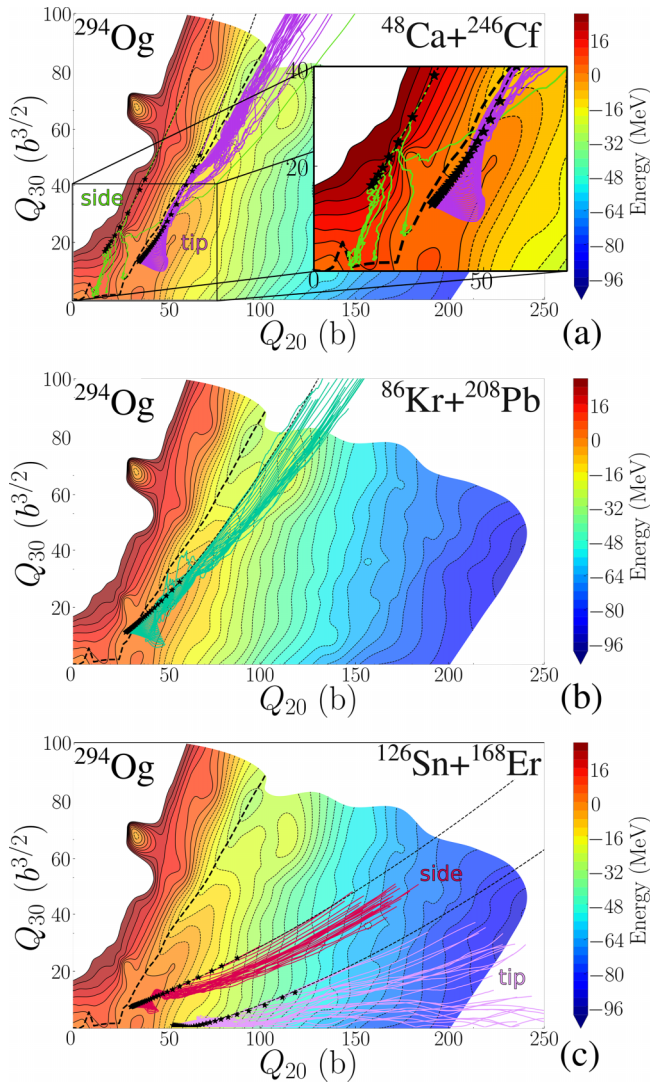


FIG. 7. Overlay of Q_{20} - Q_{30} trajectories of (a) $^{48}\text{Ca} + ^{246}\text{Cf}$, (b) $^{86}\text{Kr} + ^{208}\text{Pb}$, and (c) $^{126}\text{Sn} + ^{168}\text{Er}$ calculations on the zero-temperature PES of ^{294}Og . The dotted lines correspond to the incident kinematic trajectories, determined from TDHF, which are (quasi)identical for all reactions of the same entrance channel. Contact points (defined as neck density reaching 0.08 fm^{-3}) are represented by stars. Solid lines show the trajectories from the entry point to scission. The dashed line represents the asymmetric fission path. The inset in panel (a) is a zoom of the compact region of the PES.

$Q_{30} = 0 \text{ b}^{3/2}$) and a potential gradient essentially driving the system towards smaller asymmetries, thus trapping the system into a deformation close to the ground-state one and leading to fusion. Quasifission is found for the side orientation in a small energy range between quasielastic and fusion. In this case the entry point is located in a region of the PES with a large gradient along the Q_{20} axis [see also inset of Fig. 7(a)], driving the system towards more elongation rather than towards fusion.

The contact points for the tip orientations, however, are always more asymmetric and elongated than the second

barrier and therefore do not lead to fusion. Instead, the system remains trapped in the asymmetric valley. Although the $^{48}\text{Ca} + ^{246}\text{Cf}$ quasifission paths for the tip orientation are found at Q_{20} slightly larger than that of the asymmetric fission path (dashed line), this is an indication that the system is affected by similar shell effects in both mechanisms. Further indication can be seen from the close resemblance between the nuclear shape obtained near the entry point and the one calculated statically for the asymmetric valley [see Fig. 8, $^{48}\text{Ca} + ^{246}\text{Cf}$ tip panel].

2. $^{86}\text{Kr} + ^{208}\text{Pb}$

The Q_{20} - Q_{30} trajectories in the case of $^{86}\text{Kr} + ^{208}\text{Pb}$ collisions are shown in Fig. 7(b). The incoming trajectory essentially follows the ridge between the asymmetric valley and more symmetric modes. As a result, the contact points are also located along that ridge. As in the $^{48}\text{Ca} + ^{246}\text{Cf}$ tip orientation case, most of these contact points are located at larger elongations than the second barrier and, therefore, are not able to find a path to fusion. Only the highest center-of-mass energies lead to contact points slightly more compact than the second barrier. However, at these energies the shell effects responsible for the structures in the PES have potentially disappeared.

Finally, despite apparent initial fluctuations near the entry points that lead to some exploration of the asymmetric valley, all outgoing trajectories end up further away from the asymmetric mode than the entrance channel. As a result, there is no clear correlation between the PES and the quasifission trajectories in this system. Once again, this could be due to the larger excitation energies induced by the large initial kinetic energy necessary to overcome the stronger Coulomb barrier in more symmetric systems.

3. $^{126}\text{Sn} + ^{168}\text{Er}$

Finally, quasifission trajectories are shown for $^{126}\text{Sn} + ^{168}\text{Er}$ tip and side orientations in Fig. 7(c). The incoming trajectories explore configurations away from the symmetric and asymmetric modes. The tip orientation is associated with values of the octupole moment smaller than those of the side orientation and even leads to entry points with $Q_{30} \simeq 0$ at highest energies. Neither orientation, however, reaches more compact configurations than the second barrier. All collisions lead to quasifission with smaller Q_{30} in the exit channel. Tip orientations are even able to produce near-symmetric fragments.

Overall, no clear correlation between the PES and quasifission trajectories is observed. This could be due to the fact that the PES is relatively flat in the Q_{30} direction in the region explored by $^{126}\text{Sn} + ^{168}\text{Er}$ reactions. In addition, being the most symmetric reaction, it is also the one with the highest Coulomb barrier. As a result, the amount of excitation energy deposited into the system in the entry point is very large and could wash out shell effects.

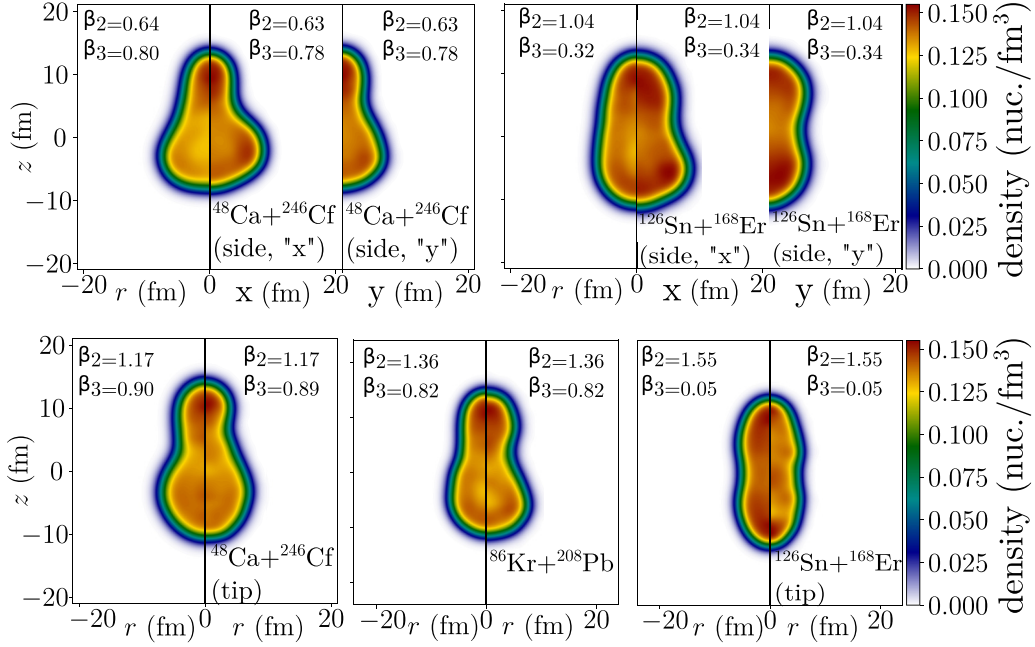


FIG. 8. Comparison of static shapes (left panels) with shapes obtained from TDHF at entry points (where neck density reaches 0.14 fm^{-3}) for several reactions and orientations. The deformation parameters of the static shapes are the ones (from the PES calculations) closest to the ones observed at the entry points. Density slices are shown in both the (x, z) and (y, z) planes in the case of side orientations. The energies of the collisions are those indicated in Fig. 9.

V. DISCUSSION

We see in Fig. 7 that the three reactions cover much of the Q_{20} - Q_{30} plane that is relevant for the PES. Naturally, this does not mean that all reactions are sensitive to the structure of the PES itself. The more symmetric collisions require more energy to overcome the Coulomb barrier. Thus, more energy is converted into excitation energy that may hinder, if not kill, shell effects and thus structures on the PES. Nevertheless, the most asymmetric reactions seem to be sensitive to these structures, such as the second barrier, direction of the gradient of the PES near the contact point, and the asymmetric valley.

We also observe that the trajectories for different entrance channels (defined as colliding nuclei with a specific orientation) essentially do not overlap with each other, despite the broad range of energies considered for each system. This indicates that the reaction mechanisms (in terms of shape evolution) are more sensitive to the initial configuration than to the energy of the collision.

Selected trajectories for each system and orientation are shown in Fig. 9. The $^{48}\text{Ca} + ^{246}\text{Cf}$ side orientation at $E_{\text{c.m.}} \simeq 220 \text{ MeV}$ leads to the longest contact time ($\approx 27 \text{ zs}$) found in the entire set of calculations. Soon after the entry point the system follows a steep descent in the PES before going towards scission [see also inset of Fig. 7(a)]. Here, the path to scission is slightly more symmetric than the asymmetric path. This could indicate that the PES is not entirely relevant for this outgoing trajectory as the latter assumes axial symmetry while the side orientation breaks this symmetry.

Indeed, the evolution of $\langle y^2 \rangle / \langle x^2 \rangle$ shown in Fig. 10 indicates that collisions with side orientations remain nonaxial during the entire reaction. (A value different than 1 is a signature for a nonaxial shape for collisions along the z axis.) Moreover, dynamical effects may take the system away from the adiabatic asymmetric path. The $^{48}\text{Ca} + ^{246}\text{Cf}$ tip orientation (which is axially symmetric for central collisions) is shown at the same energy in Fig. 9 for comparison. In this case, the outgoing trajectory essentially follows the asymmetric valley.

The $^{86}\text{Kr} + ^{208}\text{Pb}$ trajectory is shown for $E_{\text{c.m.}} \simeq 465 \text{ MeV}$. It corresponds to the largest mass transfer for this reaction (≈ 6.7 protons and ≈ 11.4 neutrons from the heavy fragment to the light one).

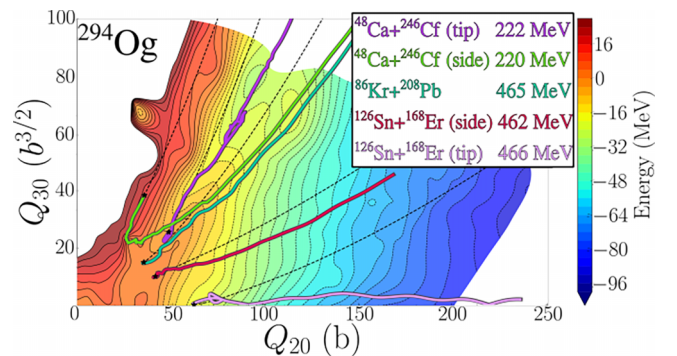


FIG. 9. Same as Fig. 7 for selected trajectories indicated in the legend.

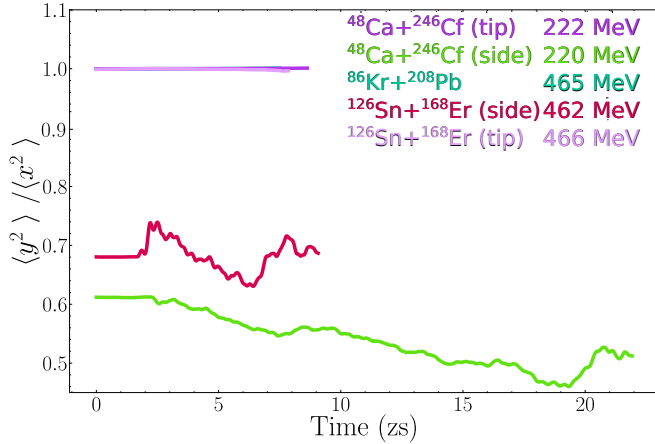


FIG. 10. Evolution of $\langle y^2 \rangle / \langle x^2 \rangle$ as a function of time for the systems considered in Fig. 9. Systems with an axial symmetry are expected to give a value of 1.

Figure 9 also shows the trajectories for the side and tip collisions of $^{126}\text{Sn} + ^{168}\text{Er}$ at $E_{\text{c.m.}} \simeq 462$ and 466 MeV, respectively. These energies also correspond to the largest charge transfer for this system: 1.8 (9.0) protons for the side (tip) orientation. Although the largest charge transfer is obtained at similar energies, the amount of transfer is very different between both orientations. In particular, transfer is hindered for side orientation at all energies, which could be due to spherical shell effects in the magic Sn ($Z = 50$) collision partner. For tip collisions, however, the entry point reaches $Q_{30} \approx 0$ and, as a result, full mass and charge equilibration is observed in the exit channel.

The quasifission trajectories in Figs. 7 and 9 are plotted up to scission, defined as the neck density becoming smaller than $\rho_0/2 = 0.08 \text{ fm}^{-3}$. We see that scission in $^{48}\text{Ca} + ^{246}\text{Cf}$ and $^{86}\text{Kr} + ^{208}\text{Pb}$ quasifission reactions occurs beyond the scission line of the PES. This does not necessarily indicate a difference between fission and quasifission mechanisms as the PES is obtained with an adiabatic approximation that breaks down near scission due to nonadiabatic dynamical effects [48]. Nonadiabatic effects are expected to affect the scission configuration in fission and quasifission in a similar way. For this reason discrepancies between shapes near scission are not of great concern. Comparing scission configurations in fission and quasifission would require full time-dependent calculations of fission dynamics [48,49,76–78] that are beyond the scope of this work. Nevertheless, we note that, in the case of $^{126}\text{Sn} + ^{168}\text{Er}$, most quasifission trajectories scission before the scission line, except for the most symmetric exit channels. This can be interpreted as an effect of the spherical magic shell at $Z = 50$ in the light fragment, leading to more compact configurations at scission. This is in agreement with the observation of higher TKE for these reactions in Fig. 4.

VI. CONCLUSION

Quasifission mechanisms have been studied with the TDHF approach in several reactions forming ^{294}Og as a compound nucleus. The exit channel strongly depends on the mass asymmetry of the collision partners, as well as on their initial orientation. However, it exhibits only a small dependence on the energy of the reaction.

Trajectories in the Q_{20} - Q_{30} plane were extracted and compared with the PESs computed for axial shapes. Properties of the most asymmetric collision ($^{48}\text{Ca} + ^{246}\text{Cf}$) could be interpreted in terms of features of the PES. In particular, the topography near the entry point determines whether the system fuses or encounters quasifission along the asymmetric valley.

Spherical shell effects associated with the $Z = 50$ magic gap could be responsible for charge equilibration hindrance in the most symmetric reaction, $^{126}\text{Sn} + ^{168}\text{Er}$, resulting in larger TKE and more compact scission configurations. Nevertheless, collisions with the tip of ^{168}Er are able to take the tin collision partner away from magicity, leading to the production of near-symmetric fragments.

More symmetric collisions require more energy to reach contact. The resulting excitation energy could wash out shell effects responsible for the structure of the PES. For these reactions, the zero-temperature PES may not be the best predictor of energy variation with shape changes. Instead a PES accounting for excitation energy could be used. Calculations of free energy variation with shape at finite temperature (see, e.g., Refs. [35,36,51,79]) show that new valleys emerge and modes change their positions within the Q_{20} - Q_{30} plane. The dissipation process outlined in Refs. [80,81] on the way to scission is also expected to affect these trajectories. In addition to finite excitation energy, it would be interesting to develop the PES at finite angular momentum for quasifission studies. Triaxiality should also be considered in the construction of the PES as it is relevant to noncentral collisions as well as reactions with deformed nuclei.

ACKNOWLEDGMENTS

The authors would like to acknowledge the valuable contributions of Rémi Bernard, especially on the calculations of potential energy surfaces. Contributions from Daniel Lee on the discussions of trajectories are acknowledged. This work has been supported by the Australian Research Council Discovery Project (Project No. DP190100256). Computational resources were provided by the Australian Government through the National Computational Infrastructure (NCI) under the ANU Merit Allocation Scheme, the Adapter Scheme, and the National Committee Merit Allocation Scheme. P.M. acknowledges the support of the Australian National University through the Deakin Ph.D. scholarship and the Dean's Merit Scholarship in science.

TABLE II. Fragments produced in $^{48}\text{Ca} + ^{246}\text{Cf}$ with the side orientation. Energies ($E_{c.m.}$ and TKE) are in MeV and contact times (Contact) are in zeptoseconds. The subscripts H and L stand for heavy and light fragments, respectively.

$E_{c.m.}$	Contact	Z_H	N_H	Z_L	N_L	TKE
199.92	0.0	97.99	147.89	20.01	28.08	196.86
206.92	1.021	97.48	147.03	20.5	28.79	186.5
209.92	2.172	96.42	146.17	21.57	29.62	185.6
214.92	14.10	81.96	123.98	36.03	51.87	239.21
219.92	26.88	69.86	105.4	48.13	70.59	239.58
233.92	Fusion					

APPENDIX: DETAILS OF TDHF RESULTS

The following tables provide details of the TDHF results used to produce the figures of the paper. The data are for primary fragments, i.e., prior to subsequent decay. Data are presented for calculations leading to two fragments in the exit channel, unless they are labeled as “fusion,” which in this context means contact times exceeding 30 zs.

TABLE III. Same as Table II for $^{48}\text{Ca} + ^{246}\text{Cf}$ with the tip orientation.

$E_{c.m.}$	Contact	Z_H	N_H	Z_L	N_L	TKE
180.08	0.0	98.02	148.04	19.98	27.94	179.01
190.08	0.883	97.8	147.6	20.19	28.32	174.49
195.08	9.892	85.06	127.97	32.93	47.78	223.37
199.08	14.55	81.92	124.24	36.07	51.6	229.36
200.08	17.27	77.87	117.31	40.12	58.54	251.53
201.08	13.70	79.86	121.15	38.13	54.66	246.26
203.08	14.63	83.34	126.96	34.66	49.03	220.83
206.08	10.85	84.5	127.14	33.5	48.82	219.59
209.08	12.19	87.11	133.0	30.89	43.0	206.7
212.08	10.45	86.27	131.5	31.73	44.49	209.65
215.08	15.10	85.16	129.07	32.84	46.93	211.36
218.08	9.968	87.19	132.58	30.81	43.41	208.02
222.08	10.16	86.87	132.08	31.13	43.91	207.63
224.08	10.14	86.87	131.99	31.13	44.0	209.21
226.08	9.988	87.02	131.83	30.98	44.17	208.34
230.08	9.956	86.94	131.89	31.05	44.1	210.67
232.08	10.14	86.67	130.83	31.33	45.16	213.55
236.08	11.43	85.32	129.64	32.68	46.35	218.52
239.07	12.42	85.8	130.13	32.2	45.86	203.42
242.07	12.00	86.05	130.49	31.95	45.51	206.76

TABLE IV. Same as Table II for $^{86}\text{Kr} + ^{208}\text{Pb}$.

$E_{c.m.}$	Contact	Z_H	N_H	Z_L	N_L	TKE
324.97	2.439	82.55	124.17	35.43	51.66	245.12
328.97	2.547	82.75	123.84	35.23	51.98	245.16
332.97	2.619	82.72	123.98	35.25	51.88	243.77
336.97	2.622	82.54	124.29	35.43	51.58	245.3
340.97	2.593	82.39	124.51	35.59	51.36	248.61
344.97	2.573	82.34	124.66	35.64	51.23	250.9
348.97	2.577	82.3	124.7	35.69	51.21	251.89
352.97	2.603	82.2	124.62	35.79	51.3	252.18
356.97	2.635	82.03	124.44	35.96	51.53	252.3
360.97	2.665	81.81	124.15	36.18	51.81	252.1
364.97	2.695	81.58	123.78	36.41	52.2	251.61
368.97	2.731	81.35	123.3	36.65	52.69	251.0
372.97	2.763	81.12	122.76	36.88	53.24	250.68
376.97	2.791	80.95	122.23	37.05	53.77	250.77
380.97	2.819	80.82	121.9	37.18	54.09	250.35
384.97	2.861	80.68	121.62	37.32	54.37	249.69
388.97	2.915	80.48	121.4	37.52	54.6	248.65
392.97	2.963	80.2	121.2	37.8	54.8	246.98
396.97	3.008	79.87	120.97	38.13	55.03	244.69
400.97	3.066	79.55	120.67	38.45	55.33	242.56
404.97	3.144	79.17	120.17	38.83	55.83	242.44
408.97	3.190	78.78	119.6	39.21	56.4	244.35
412.96	3.211	78.43	119.0	39.57	56.99	245.66
416.96	3.226	78.16	118.58	39.84	57.41	248.04
420.96	3.240	77.96	118.32	40.04	57.67	249.03
424.96	3.253	77.82	118.15	40.18	57.85	248.92
428.96	3.268	77.65	118.0	40.35	58.0	249.79
432.96	3.286	77.48	117.77	40.52	58.22	249.02
436.96	3.322	77.18	117.33	40.82	58.66	247.46
440.96	3.385	76.69	116.69	41.3	59.31	250.28
444.96	3.403	76.2	115.92	41.8	60.07	253.35
448.96	3.427	75.85	115.06	42.15	60.93	250.8
452.96	3.513	75.6	114.76	42.4	61.23	248.41
456.96	3.674	75.41	114.63	42.59	61.37	245.53
460.96	3.711	75.34	114.6	42.66	61.4	246.32
464.96	3.736	75.29	114.57	42.71	61.43	248.0
469.96	3.809	75.42	114.73	42.58	61.26	247.35
474.96	3.872	75.9	115.57	42.09	60.42	244.0
479.96	3.907	76.87	116.88	41.13	59.11	245.1
484.96	3.850	77.27	117.19	40.73	58.81	249.53
489.96	3.821	77.45	117.04	40.55	58.95	252.7
499.96	3.807	77.69	116.86	40.31	59.13	255.22
519.95	3.760	77.53	116.41	40.46	59.58	264.82
539.95	3.699	77.91	117.4	40.08	58.6	261.42
559.95	3.600	77.98	118.06	40.02	57.94	253.03
569.95	3.553	78.57	118.58	39.43	57.42	244.83
579.95	3.476	79.5	119.21	38.51	56.79	243.14
584.95	3.507	79.98	119.65	38.02	56.35	236.79
589.95	3.594	79.42	119.24	38.57	56.75	240.78
599.95	3.685	77.57	118.09	40.43	57.9	252.35
609.94	4.403	76.68	115.13	41.32	60.87	246.15
619.94	5.266	75.86	115.26	42.14	60.73	245.43
629.94	5.982	80.22	119.49	37.78	56.51	228.06

TABLE V. Same as Table II for $^{126}\text{Sn} + ^{168}\text{Er}$ with the side orientation.

$E_{c.m.}$	Contact	Z_H	N_H	Z_L	N_L	TKE
331.89	0.0	67.98	99.97	50.01	75.99	330.43
341.89	0.216	67.87	100.07	50.12	75.78	326.79
351.89	1.106	67.99	101.3	49.99	74.53	292.72
361.89	1.678	68.04	102.21	49.94	73.63	285.27
371.88	2.056	67.77	100.99	50.21	74.86	290.15
381.88	2.447	67.07	100.21	50.92	75.66	285.69
391.88	2.871	67.13	100.38	50.86	75.51	284.61
401.88	3.289	66.73	99.94	51.26	75.95	286.81
411.88	3.793	66.91	99.48	51.08	76.46	282.51
421.88	4.233	66.68	99.72	51.32	76.25	283.43
431.88	4.347	66.51	99.5	51.48	76.36	283.86
441.88	4.503	66.73	100.25	51.27	75.75	279.81
451.88	4.605	66.44	100.0	51.56	76.0	276.93
461.87	4.711	66.16	99.15	51.84	76.85	273.46
471.87	4.852	66.49	99.38	51.51	76.61	270.57
481.87	5.000	67.37	100.88	50.62	75.11	270.78
491.87	5.171	67.21	101.21	50.79	74.78	271.87
501.87	5.403	67.18	100.82	50.82	75.17	270.73
511.87	5.495	67.27	100.51	50.73	75.48	271.07
521.87	5.638	66.97	100.17	51.03	75.83	268.88
531.87	5.886	66.5	99.68	51.5	76.32	266.03
541.87	6.301	66.81	99.54	51.19	76.45	266.06
551.86	6.706	66.71	99.62	51.29	76.38	260.17
561.86	7.018	66.72	100.05	51.28	75.94	263.72
571.86	7.429	67.06	100.51	50.94	75.48	260.9
581.86	7.453	67.11	100.11	50.88	75.88	261.59
591.86	7.212	67.06	100.33	50.94	75.66	265.02
601.86	6.905	66.94	100.2	51.06	75.8	264.47
611.86	6.632	66.14	99.09	51.86	76.91	270.67

TABLE VI. Same as Table II for $^{126}\text{Sn} + ^{168}\text{Er}$ with the tip orientation.

$E_{c.m.}$	Contact	Z_H	N_H	Z_L	N_L	TKE
306.14	0.0	67.98	99.96	50.01	76.0	304.97
316.14	0.495	67.72	99.96	50.27	75.86	294.31
326.14	1.445	67.3	99.5	50.68	76.28	268.16
336.13	1.732	66.99	99.65	51.01	76.21	277.18
346.13	2.354	66.1	98.63	51.89	77.23	259.25
356.13	2.621	65.72	97.68	52.27	78.18	254.28
366.13	2.787	66.0	98.28	51.99	77.56	246.9
376.13	3.347	63.88	94.43	54.11	81.49	237.35
386.13	3.457	61.12	92.09	56.87	83.81	237.67
396.13	3.279	62.71	91.97	55.28	83.95	236.52
406.13	2.766	65.59	96.59	52.4	79.33	251.93
416.13	2.702	65.49	96.73	52.51	79.25	251.03
426.12	2.675	65.25	96.62	52.75	79.37	250.66
436.12	2.795	65.02	97.05	52.98	78.94	243.81
446.12	3.212	66.14	99.48	51.86	76.52	229.96
456.12	3.583	61.06	90.76	56.94	85.24	234.29
466.12	3.325	59.0	88.3	59.0	87.69	234.5
476.12	3.174	60.27	89.55	57.73	86.45	239.57
486.12	3.377	59.63	89.38	58.37	86.62	225.88
496.12	3.338	60.81	90.78	57.19	85.22	230.89
506.12	3.360	59.97	89.61	58.03	86.39	231.52
516.11	3.373	59.08	88.47	58.92	87.52	232.58
526.11	3.380	61.19	90.6	56.81	85.39	234.78
536.11	3.423	61.48	91.19	56.52	84.81	242.17
546.11	3.497	61.35	91.51	56.65	84.49	242.16
556.11	3.537	62.22	93.07	55.78	82.93	240.78
566.11	3.771	63.01	94.7	54.99	81.3	231.24
576.11	3.691	64.78	96.98	53.22	79.02	232.74

- [1] A. N. Andreyev, K. Nishio, and K.-H. Schmidt, Nuclear fission: a review of experimental advances and phenomenology, *Rep. Prog. Phys.* **81**, 016301 (2017).
- [2] K.-H. Schmidt and B. Jurado, Review on the progress in nuclear fission—experimental methods and theoretical descriptions, *Rep. Prog. Phys.* **81**, 106301 (2018).
- [3] S. Goriely, The fundamental role of fission during r-process nucleosynthesis in neutron star mergers, *Eur. Phys. J. A* **51**, 22 (2015).
- [4] D. N. Poenaru, R. A. Gherghescu, and W. Greiner, Heavy-Particle Radioactivity of Superheavy Nuclei, *Phys. Rev. Lett.* **107**, 062503 (2011).
- [5] Y. L. Zhang and Y. Z. Wang, Systematic study of cluster radioactivity of superheavy nuclei, *Phys. Rev. C* **97**, 014318 (2018).
- [6] K. P. Santhosh and C. Nithya, Systematic studies of α and heavy-cluster emissions from superheavy nuclei, *Phys. Rev. C* **97**, 064616 (2018).
- [7] M. Warda, A. Zdeb, and L. M. Robledo, Cluster radioactivity in superheavy nuclei, *Phys. Rev. C* **98**, 041602(R) (2018).
- [8] Z. Matheson, S. A. Giuliani, W. Nazarewicz, J. Sadhukhan, and N. Schunck, Cluster radioactivity of $^{294}_{118}\text{Og}_{176}$, *Phys. Rev. C* **99**, 041304(R) (2019).
- [9] C. Ishizuka, X. Zhang, M. D. Usang, F. A. Ivanyuk, and S. Chiba, Effect of the doubly magic shell closures in ^{132}Sn and ^{208}Pb on the mass distributions of fission fragments of superheavy nuclei, *Phys. Rev. C* **101**, 011601(R) (2020).
- [10] A. Jain, R. Sharma, S. K. Jain, P. K. Sharma, and G. Saxena, Cluster radioactivity in $^{294,296}\text{Og}$, *Hyperfine Interact.* **242**, 60 (2021).
- [11] K. Banerjee, D. J. Hinde, M. Dasgupta, J. Sadhukhan, E. C. Simpson, D. Y. Jeung, C. Simenel, B. M. A. Swinton-Bland, E. Williams, L. T. Bezzina, I. P. Carter, K. J. Cook, H. M. Albers, Ch. E. Düllmann, J. Khuyagbaatar, B. Kindler, B. Lommel, C. Mokry, E. Prasad, J. Runke *et al.*, Sensitive search for near-symmetric and super-asymmetric fusion-fission of the superheavy element Flerovium ($Z=114$), *Phys. Lett. B* **820**, 136601 (2021).
- [12] N. Schunck and L. M. Robledo, Microscopic theory of nuclear fission: A review, *Rep. Prog. Phys.* **79**, 116301 (2016).
- [13] M. Bender, R. Bernard, G. Bertsch, S. Chiba, J. J. Dobaczewski, N. Dubray, S. Giuliani, K. Hagino, D. Lacroix, Z. Li, P. Magierski, J. Maruhn, W. Nazarewicz, J. Pei, S. Péru-Desenfans, N. Pillet, J. Randrup, D. Regnier, P.-G. Reinhard, L. M. Robledo *et al.*, Future of nuclear fission theory, *J. Phys. G: Nucl. Part. Phys.* **47**, 113002 (2020).

- [14] C. Gustafsson, P. Möller, and S. G. Nilsson, The microscopic mechanism behind the fission barrier asymmetry, *Phys. Lett. B* **34**, 349 (1971).
- [15] S. Ćwiok, W. Nazarewicz, J. X. Saladin, W. Płóciennik, and A. Johnson, Hyperdeformations and clustering in the actinide nuclei, *Phys. Lett. B* **322**, 304 (1994).
- [16] M. Brack, J. Damgaard, A. S. Jensen, H. C. Pauli, V. M. Strutinsky, and C. Y. Wong, Funny hills: The shell-correction approach to nuclear shell effects and its applications to the fission process, *Rev. Mod. Phys.* **44**, 320 (1972).
- [17] R. N. Bernard, C. Simenel, and G. Blanchon, Hartree–Fock–Bogoliubov study of quantum shell effects on the path to fission in ^{180}Hg , ^{236}U , and ^{256}Fm , *Eur. Phys. J. A* **59**, 51 (2023).
- [18] B. D. Wilkins, E. P. Steinberg, and R. R. Chasman, Scission-point model of nuclear-fission based on deformed-shell effects, *Phys. Rev. C* **14**, 1832 (1976).
- [19] G. Scamps and C. Simenel, Impact of pear-shaped fission fragments on mass-asymmetric fission in actinides, *Nature (London)* **564**, 382 (2018).
- [20] M. G. Itkis, J. Äystö, S. Beghini, A. A. Bogachev, L. Corradi, O. Dorvaux, A. Gadea, G. Giardina, F. Hanappe, I. M. Itkis, M. Jandel, J. Kliman, S. V. Khlebnikov, G. N. Kniajeva, N. A. Kondratiev, E. M. Kozulin, L. Krupa, A. Latina, T. Materna, G. Montagnoli *et al.*, Shell effects in fission and quasi-fission of heavy and superheavy nuclei, *Nucl. Phys. A* **734**, 136 (2004).
- [21] V. Zagrebaev and W. Greiner, Unified consideration of deep inelastic, quasi-fission and fusion-fission phenomena, *J. Phys. G: Nucl. Part. Phys.* **31**, 825 (2005).
- [22] K. Nishio, H. Ikezoe, S. Mitsuoka, I. Nishinaka, Y. Nagame, Y. Watanabe, T. Ohtsuki, K. Hirose, and S. Hofmann, Effects of nuclear orientation on the mass distribution of fission fragments in the reaction of $^{36}\text{S} + ^{238}\text{U}$, *Phys. Rev. C* **77**, 064607 (2008).
- [23] E. M. Kozulin, G. N. Knyazheva, S. N. Dmitriev, I. M. Itkis, M. G. Itkis, T. A. Loktev, K. V. Novikov, A. N. Baranov, W. H. Trzaska, E. Vardaci, S. Heinz, O. Beliuskina, and S. V. Khlebnikov, Shell effects in damped collisions of ^{88}Sr with ^{176}Yb at the Coulomb barrier energy, *Phys. Rev. C* **89**, 014614 (2014).
- [24] A. Wakhle, C. Simenel, D. J. Hinde, M. Dasgupta, M. Evers, D. H. Luong, R. du Rietz, and E. Williams, Interplay between Quantum Shells and Orientation in Quasifission, *Phys. Rev. Lett.* **113**, 182502 (2014).
- [25] M. Morjean, D. J. Hinde, C. Simenel, D. Y. Jeung, M. Airiau, K. J. Cook, M. Dasgupta, A. Drouart, D. Jacquet, S. Kalkal, C. S. Palshetkar, E. Prasad, D. Rafferty, E. C. Simpson, L. Tassan-Got, K. Vo-Phuoc, and E. Williams, Evidence for the Role of Proton Shell Closure in Quasifission Reactions from X-Ray Fluorescence of Mass-Identified Fragments, *Phys. Rev. Lett.* **119**, 222502 (2017).
- [26] D. J. Hinde, D. Y. Jeung, E. Prasad, A. Wakhle, M. Dasgupta, M. Evers, D. H. Luong, R. du Rietz, C. Simenel, E. C. Simpson, and E. Williams, Sub-barrier quasifission in heavy element formation reactions with deformed actinide target nuclei, *Phys. Rev. C* **97**, 024616 (2018).
- [27] J. Töke, R. Bock, G. X. Dai, A. Gobbi, S. Gralla, K. D. Hildenbrand, J. Kuzminski, W. F. J. Müller, A. Olmi, H. Stelzer, B. B. Back, and S. Bjørnholm, Quasi-fission: The mass-drift mode in heavy-ion reactions, *Nucl. Phys. A* **440**, 327 (1985).
- [28] R. du Rietz, E. Williams, D. J. Hinde, M. Dasgupta, M. Evers, C. J. Lin, D. H. Luong, C. Simenel, and A. Wakhle, Mapping quasifission characteristics and timescales in heavy element formation reactions, *Phys. Rev. C* **88**, 054618 (2013).
- [29] C. Simenel, K. Godbey, and A. S. Umar, Timescales of Quantum Equilibration, Dissipation and Fluctuation in Nuclear Collisions, *Phys. Rev. Lett.* **124**, 212504 (2020).
- [30] D. J. Hinde, M. Dasgupta, and E. C. Simpson, Experimental studies of the competition between fusion and quasifission in the formation of heavy and superheavy nuclei, *Prog. Part. Nucl. Phys.* **118**, 103856 (2021).
- [31] A. Yu. Chizhov, M. G. Itkis, I. M. Itkis, G. N. Kniajeva, E. M. Kozulin, N. A. Kondratiev, I. V. Pokrovsky, R. N. Sagaidak, V. M. Voskressensky, A. V. Yeremin, L. Corradi, A. Gadea, A. Latina, A. M. Stefanini, S. Szilner, M. Trotta, A. M. Vinodkumar, S. Beghini, G. Montagnoli, F. Scarlassara *et al.*, Unexpected entrance-channel effect in the fission of $^{216}\text{Ra}^*$, *Phys. Rev. C* **67**, 011603(R) (2003).
- [32] R. Rafiei, R. G. Thomas, D. J. Hinde, M. Dasgupta, C. R. Morton, L. R. Gasques, M. L. Brown, and M. D. Rodriguez, Strong evidence for quasifission in asymmetric reactions forming ^{202}Po , *Phys. Rev. C* **77**, 024606 (2008).
- [33] E. Williams, D. J. Hinde, M. Dasgupta, R. du Rietz, I. P. Carter, M. Evers, D. H. Luong, S. D. McNeil, D. C. Rafferty, K. Ramachandran, and A. Wakhle, Evolution of signatures of quasifission in reactions forming curium, *Phys. Rev. C* **88**, 034611 (2013).
- [34] C. Simenel, P. McGlynn, A. S. Umar, and K. Godbey, Comparison of fission and quasi-fission modes, *Phys. Lett. B* **822**, 136648 (2021).
- [35] J. D. McDonnell, W. Nazarewicz, J. A. Sheikh, A. Staszczak, and M. Warda, Excitation-energy dependence of fission in the mercury region, *Phys. Rev. C* **90**, 021302(R) (2014).
- [36] J. Zhao, T. Nikšić, D. Vretenar, and S.-G. Zhou, Microscopic self-consistent description of induced fission dynamics: Finite-temperature effects, *Phys. Rev. C* **99**, 014618 (2019).
- [37] P.-G. Reinhard, B. Schuetrumpf, and J. A. Maruhn, The axial Hartree-Fock + BCS code SkyAx, *Comput. Phys. Commun.* **258**, 107603 (2021).
- [38] Ka-Hae Kim, T. Otsuka, and P. Bonche, Three-dimensional TDHF calculations for reactions of unstable nuclei, *J. Phys. G: Nucl. Part. Phys.* **23**, 1267 (1997).
- [39] N. Dubray, H. Goutte, and J.-P. Delaroche, Structure properties of ^{226}Th and $^{256,258,260}\text{Fm}$ fission fragments: Mean-field analysis with the Gogny force, *Phys. Rev. C* **77**, 014310 (2008).
- [40] J. A. Maruhn, P.-G. Reinhard, P. D. Stevenson, and A. S. Umar, The TDHF code Sky3D, *Comput. Phys. Commun.* **185**, 2195 (2014).
- [41] B. Schuetrumpf, P.-G. Reinhard, P. D. Stevenson, A. S. Umar, and J. A. Maruhn, The TDHF code Sky3D version 1.1, *Comput. Phys. Commun.* **229**, 211 (2018).
- [42] J. W. Negele, The mean-field theory of nuclear-structure and dynamics, *Rev. Mod. Phys.* **54**, 913 (1982).
- [43] C. Simenel, Nuclear quantum many-body dynamics, *Eur. Phys. J. A* **48**, 152 (2012).
- [44] C. Simenel and A. S. Umar, Heavy-ion collisions and fission dynamics with the time-dependent Hartree-Fock theory and its extensions, *Prog. Part. Nucl. Phys.* **103**, 19 (2018).
- [45] K. Sekizawa, TDHF theory and its extensions for the multi-nucleon transfer reaction: A mini review, *Front. Phys.* **7**, 20 (2019).

- [46] P. D. Stevenson and M. C. Barton, Low-energy heavy-ion reactions and the Skyrme effective interaction, *Prog. Part. Nucl. Phys.* **104**, 142 (2019).
- [47] K. Godbey and A. S. Umar, Quasifission dynamics in microscopic theories, *Front. Phys.* **8**, 40 (2020).
- [48] C. Simenel and A. S. Umar, Formation and dynamics of fission fragments, *Phys. Rev. C* **89**, 031601(R) (2014).
- [49] G. Scamps, C. Simenel, and D. Lacroix, Superfluid dynamics of ^{258}Fm fission, *Phys. Rev. C* **92**, 011602(R) (2015).
- [50] Y. Tanimura, D. Lacroix, and S. Ayik, Microscopic Phase-Space Exploration Modeling of ^{258}Fm Spontaneous Fission, *Phys. Rev. Lett.* **118**, 152501 (2017).
- [51] B. Li, D. Vretenar, Z. X. Ren, T. Nikšić, J. Zhao, P. W. Zhao, and J. Meng, Fission dynamics, dissipation, and clustering at finite temperature, *Phys. Rev. C* **107**, 014303 (2023).
- [52] P. Jachimowicz, M. Kowal, and J. Skalski, Adiabatic fission barriers in superheavy nuclei, *Phys. Rev. C* **95**, 014303 (2017).
- [53] W. Ryssens, M. Bender, K. Bennaceur, P.-H. Heenen, and J. Meyer, Impact of the surface energy coefficient on the deformation properties of atomic nuclei as predicted by Skyrme energy density functionals, *Phys. Rev. C* **99**, 044315 (2019).
- [54] E. K. Hulet, J. F. Wild, R. J. Dougan, R. W. Lougheed, J. H. Landrum, A. D. Dougan, M. Schadel, R. L. Hahn, P. A. Baisden, C. M. Henderson, R. J. Dupzyk, K. Sümmerer, and G. R. Bethune, Bimodal Symmetric Fission Observed in the Heaviest Elements, *Phys. Rev. Lett.* **56**, 313 (1986).
- [55] W. J. Świątecki, K. Siwek-Wilczyńska, and J. Wilczyński, Fusion by diffusion. II. Synthesis of transfermium elements in cold fusion reactions, *Phys. Rev. C* **71**, 014602 (2005).
- [56] V. E. Oberacker, A. S. Umar, and C. Simenel, Dissipative dynamics in quasifission, *Phys. Rev. C* **90**, 054605 (2014).
- [57] A. S. Umar, V. E. Oberacker, and C. Simenel, Fusion and quasifission dynamics in the reactions $^{48}\text{Ca} + ^{249}\text{Bk}$ and $^{50}\text{Ti} + ^{249}\text{Bk}$ using a time-dependent Hartree-Fock approach, *Phys. Rev. C* **94**, 024605 (2016).
- [58] A. S. Umar, V. E. Oberacker, and C. Simenel, Shape evolution and collective dynamics of quasifission in the time-dependent Hartree-Fock approach, *Phys. Rev. C* **92**, 024621 (2015).
- [59] K. Hammerton, Z. Kohley, D. J. Hinde, M. Dasgupta, A. Wakhle, E. Williams, V. E. Oberacker, A. S. Umar, I. P. Carter, K. J. Cook, J. Greene, D. Y. Jeung, D. H. Luong, S. D. McNeil, C. S. Palshetkar, D. C. Rafferty, C. Simenel, and K. Stiefel, Reduced quasifission competition in fusion reactions forming neutron-rich heavy elements, *Phys. Rev. C* **91**, 041602(R) (2015).
- [60] K. Sekizawa and K. Yabana, Time-dependent Hartree-Fock calculations for multinucleon transfer and quasifission processes in the $^{64}\text{Ni} + ^{238}\text{U}$ reaction, *Phys. Rev. C* **93**, 054616 (2016).
- [61] L. Guo, C. Shen, C. Yu, and Z. Wu, Isotopic trends of quasifission and fusion-fission in the reactions $^{48}\text{Ca} + ^{239,244}\text{Pu}$, *Phys. Rev. C* **98**, 064609 (2018).
- [62] H. Zheng, S. Burrello, M. Colonna, D. Lacroix, and G. Scamps, Connecting the nuclear equation of state to the interplay between fusion and quasifission processes in low-energy nuclear reactions, *Phys. Rev. C* **98**, 024622 (2018).
- [63] K. Godbey, A. S. Umar, and C. Simenel, Deformed shell effects in $^{48}\text{Ca} + ^{249}\text{Bk}$ quasifission fragments, *Phys. Rev. C* **100**, 024610 (2019).
- [64] O. Yilmaz, G. Turan, and B. Yilmaz, Quasi-fission and fusion-fission reactions in $^{48}\text{Ca} + ^{208}\text{Pb}$ collisions at $E_{\text{c.m.}} = 190$ MeV, *Eur. Phys. J. A* **56**, 37 (2020).
- [65] L. Li, L. Guo, K. Godbey, and A. S. Umar, Impact of tensor force on quantum shell effects in quasifission reactions, *Phys. Lett. B* **833**, 137349 (2022).
- [66] Z. Wu, L. Guo, Z. Liu, and G. Peng, Production of proton-rich nuclei in the vicinity of ^{100}Sn via multinucleon transfer reactions, *Phys. Lett. B* **825**, 136886 (2022).
- [67] D. J. Hinde, D. Hilscher, H. Rossner, B. Gebauer, M. Lehmann, and M. Wilpert, Neutron emission as a probe of fusion-fission and quasi-fission dynamics, *Phys. Rev. C* **45**, 1229 (1992).
- [68] V. E. Viola, K. Kwiatkowski, and M. Walker, Systematics of fission fragment total kinetic-energy release, *Phys. Rev. C* **31**, 1550 (1985).
- [69] D. J. Hinde, J. R. Leigh, J. J. M. Bokhorst, J. O. Newton, R. L. Walsh, and J. W. Boldeman, Mass-split dependence of the pre- and post-scission neutron multiplicities for fission of ^{251}Es , *Nucl. Phys. A* **472**, 318 (1987).
- [70] V. I. Zagrebaev, Yu. Ts. Oganessian, M. G. Itkis, and W. Greiner, Superheavy nuclei and quasi-atoms produced in collisions of transuranium ions, *Phys. Rev. C* **73**, 031602(R) (2006).
- [71] D. J. Kedziora and C. Simenel, New inverse quasifission mechanism to produce neutron-rich transfermium nuclei, *Phys. Rev. C* **81**, 044613 (2010).
- [72] P. A. Butler and W. Nazarewicz, Intrinsic reflection asymmetry in atomic nuclei, *Rev. Mod. Phys.* **68**, 349 (1996).
- [73] A. O. Macchiavelli, J. Burde, R. M. Diamond, C. W. Beausang, M. A. Deleplanque, R. J. McDonald, F. S. Stephens, and J. E. Draper, Superdeformation in $^{104,105}\text{Pd}$, *Phys. Rev. C* **38**, 1088 (1988).
- [74] W. Nazarewicz, J. Dudek, R. Bengtsson, T. Bengtsson, and I. Ragnarsson, Microscopic study of the high-spin behaviour in selected $A \simeq 80$ nuclei, *Nucl. Phys. A* **435**, 397 (1985).
- [75] G. Scamps and C. Simenel, Effect of shell structure on the fission of sub-lead nuclei, *Phys. Rev. C* **100**, 041602(R) (2019).
- [76] P. M. Goddard, P. D. Stevenson, and A. Rios, Fission dynamics within time-dependent Hartree-Fock: Deformation-induced fission, *Phys. Rev. C* **92**, 054610 (2015).
- [77] A. Bulgac, P. Magierski, K. J. Roche, and I. Stetcu, Induced Fission of ^{240}Pu within a Real-Time Microscopic Framework, *Phys. Rev. Lett.* **116**, 122504 (2016).
- [78] Z. X. Ren, J. Zhao, D. Vretenar, T. Nikšić, P. W. Zhao, and J. Meng, Microscopic analysis of induced nuclear fission dynamics, *Phys. Rev. C* **105**, 044313 (2022).
- [79] J. C. Pei, W. Nazarewicz, J. A. Sheikh, and A. K. Kerman, Fission Barriers of Compound Superheavy Nuclei, *Phys. Rev. Lett.* **102**, 192501 (2009).
- [80] J. Zhao, T. Nikšić, and D. Vretenar, Time-dependent generator coordinate method study of fission: Dissipation effects, *Phys. Rev. C* **105**, 054604 (2022).
- [81] J. Zhao, T. Nikšić, and D. Vretenar, Time-dependent generator coordinate method study of fission. II. Total kinetic energy distribution, *Phys. Rev. C* **106**, 054609 (2022).